Nano Research

ISSN 1998-0124 CN 11-5974/O4
https://doi.org/10.1007/s12274-022-5080-1

Research Article

Amplitude-mode spectroscopy of chemically injected and photogenerated charge carriers in semiconducting single-walled carbon nanotubes

Shai R. Vardeny[1], Alan Phillips[2,3], Kira A. Thurman[2], Z. Valy Vardeny[4], and Jeffrey L. Blackburn[2] (✉)

[1] *Division of Electrical, Electronic, and Infocommunications Engineering, Osaka University, 2-1 Yamada-oka, Suita, Osaka 565-0871, Japan*
[2] *Materials, Chemistry, and Computation Science Directorate, National Renewable Energy Laboratory, Golden, CO 80401, USA*
[3] *Department of Physics, Colorado School of Mines, Golden, CO 80401, USA*
[4] *Department of Physics & Astronomy, University of Utah, Salt Lake City, UT 84112, USA*

Received: 10 July 2022 / **Revised:** 13 September 2022 / **Accepted:** 20 September 2022

ABSTRACT

In one-dimensional semiconductors such as conjugated polymers and semiconducting single-walled carbon nanotubes (s-SWCNTs), injected charge carriers (electrons or holes) can have profound impacts on both electronic conductivity and optical spectra, even at low carrier densities. Understanding charge-related spectral features is a key fundamental challenge with important technological implications. Here, we employ a systematic suite of experimental and theoretical tools to understand the mid-infrared charge signatures of heavily p-type doped polymer-wrapped s-SWCNTs. Across a broad range of nanotube diameters, we find that hole charge carriers induce strong Fano anti-resonances in mid-infrared transmission spectra that correspond to defect-related (D-band) and in-plane tangential (G-band) Raman-active vibrational modes, along with anti-resonances arising from infrared (IR)-active polymer and SWCNT modes. We employ ^{13}C isotope-labeled s-SWCNTs and a removable wrapping polymer to clarify the relative intensities, energies, and sources of all observed anti-resonances. Simulations performed with the "amplitude mode model" are used to quantitatively reproduce Raman spectra and also help to explain the outsized intensity of the D-band anti-resonance, relative to the G-band, observed for both moderately and degenerately doped s-SWCNTs. The results provide a framework for future studies of ground- and excited-state charge carriers in s-SWCNTs and a variety of low-dimensional materials.

KEYWORDS

carbon nanotubes, doping, charge carriers, phonons, electron-phonon coupling

1 Introduction

π-conjugated semiconductors, such as semiconducting polymers and single-walled carbon nanotubes (s-SWCNTs), hold promise for enabling the next generation of flexible, conformal, and lightweight optoelectronic devices. Technologies such as photovoltaics [1], thermoelectrics [2], digital logic [3], and electronic ratchets [4] rely upon the generation, transport, and interconversion of electronic charge carriers (i.e., electrons and holes) [5]. Optical spectroscopy is a powerful tool for understanding the detailed physics of charge carrier populations and key spectroscopic signatures of charges have been identified in various regions of the electromagnetic spectrum for s-SWCNTs [6–11] and other organic semiconductors [12, 13].

Charge-related signatures in s-SWCNTs include the bleach of the first excitonic transition (S_{11}), an induced absorption 100–200 meV below S_{11}, Stark-related shifts of higher energy excitonic transitions, and strong free carrier absorption in the mid- to far-infrared [6, 11]. In general, charges in s-SWCNTs appear to be more characteristic of delocalized "free" charges compared to the relatively localized polarons of small molecules and semiconducting polymers, leading to some interesting differences in both transport phenomena and optical spectra [14]. Despite these important findings, much remains to be learned about electrons and holes in s-SWCNTs, including the roles of electron–phonon coupling, the degree of carrier (de)localization, and specific carrier density-dependent transport mechanisms.

In this study, we explore the spectroscopic signatures of charge carriers in highly enriched (6,5) s-SWCNTs in the infrared (IR) region and the coupling of these charges to vibrational modes. The amplitude mode model is a powerful technique for analyzing strongly coupled phonons in one-dimensional (1D) semiconductors such as π-conjugated polymers [15–25]. The amplitude mode model was first used to describe amplitude modes and phase modes of charge density wave compounds [15]. Later it was successfully introduced to π-conjugated polymers by Horovitz and collaborators [16–21], where it has been extensively used to study the phonon renormalized frequencies upon charge carrier doping and photogeneration. Recently, it has been recognized in semiconducting polymers, graphene, and SWCNTs that if phonon frequencies are close to the electronic transitions of charge carriers then the renormalized phonons appear in the IR absorption spectrum as anti-resonances, or Fano resonances on

Address correspondence to Jeffrey.Blackburn@nrel.gov

top of the electronic transition spectrum [24, 25]. Lapointe et al. demonstrated that the G- and D-band anti-resonance intensities scale with carrier density and defect density in both graphene and SWCNTs [26, 27]. Since the amplitude mode model has successfully captured the physics giving rise to anti-resonances in the IR spectra of semiconducting polymers, it is natural to translate this model to similar spectral features observed for doped s-SWCNTs, an analogous 1D nanoscale semiconductor.

Here, we utilize the amplitude mode model to characterize the quantum interference between hole charge carriers and vibrational modes in p-type (6,5) and large-diameter laser vaporization (LV) s-SWCNT thin films. Holes that are injected either by chemical doping [28] or are photogenerated by exciton dissociation across a type-II interface [29] produce an identical series of discrete Fano-like anti-resonances superimposed on the broad free carrier absorbance. The use of isotopically tuned LV ^{13}C s-SWCNTs and a removable wrapping polymer helps to confirm separate anti-resonances arriving from both s-SWCNTs and the polyfluorene wrapping polymer. We also find that for all s-SWCNT source materials and diameters studied, the intensity ratio of the defect-related D-band to the in-plane G-band is much larger in the Fourier transform infrared (FTIR) anti-resonance spectra than in Raman spectra, even for degenerately doped and highly conducting s-SWCNT networks. The amplitude mode model can quantitatively reproduce the isotope-dependent Raman scattering spectra of both (6,5) and LV s-SWCNTs, and qualitatively reproduce the large D/G ratios in anti-resonance spectra by considering the dispersion of each Raman mode. In doing so, the amplitude mode model allows for the estimation of the dispersion of the D band Raman feature.

2 Experimental

We first probe the spectroscopic signatures of positive charge carriers (holes) injected into highly enriched (6,5) s-SWCNT networks by chemical dopants, specifically triethyloxonium hexachloroantimonate (OA). The (6,5) s-SWCNTs are selectively dispersed by the wrapping polymer poly[(9,9-dioctylfluorenyl-2,7-diyl)-alt-co-(6,60-(2,20-bipyridine))] (PFO-BPy). Hole injection into the (6,5) s-SWCNT network by the adsorbed redox dopants leads to both substantial electrical conductivity and several distinct spectroscopic changes [6, 28]. In the near infrared (NIR) region (Fig. 1(a)), the lowest energy (S_{11}) excitonic transition is quenched, due to phase space filling, and a new low-energy absorption is induced (X^+) that has been attributed to the lowest-energy optical transition of trions (charged excitons) [30]. At lower energy, in the mid-IR region of the spectrum (Fig. 1(b)), a strong free-carrier absorption rises progressively to lower energies. Superimposed on this free-carrier absorption are a number of relatively sharp "negative" features (i.e., reduced absorption relative to the free carrier absorption background). As detailed previously for doped graphene [27], unsorted SWCNT networks [26], and (6,5) s-SWCNT networks [7], several of these negative features can be assigned to Fano resonances that arise from coupling of discrete Raman-active (but IR-inactive) vibrational modes to the broad spectral continuum of the injected free carriers.

As observed previously, the Fano resonances observed for the chemically doped (6,5) s-SWCNTs are all induced transparencies or "antiresonances". Rich spectral detail in the anti-resonances can be directly correlated to strong Raman modes (inset of Fig. 1(b)), particularly the multi-peak structures of both the G-band region between ca. 1,500–1,600 cm^{-1} and D-band region between ca. 1,150–1,300 cm^{-1}. The D-band region is bathochromically shifted, relative to the Raman spectrum, due to the dispersive nature of these modes with excitation wavelength (*vida infra*). Two intense

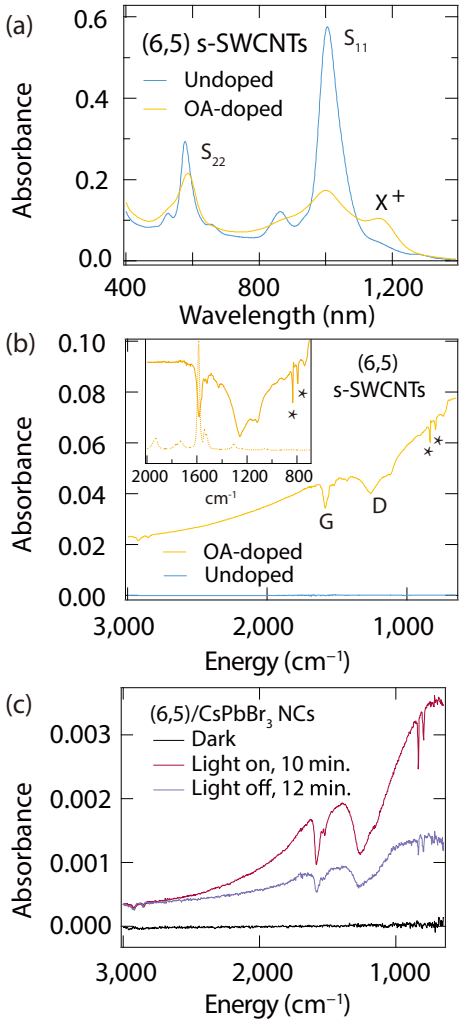

Figure 1 (a) Ultraviolet–visible (UV–Vis) and (b) FTIR absorbance spectra for undoped and heavily p-type (6,5) s-SWCNT film. The inset of (b) compares the anti-resonance observed in FTIR (solid line, free carrier absorption subtracted) with the Raman spectrum (dashed). (c) FTIR absorbance spectra of (6,5) s-SWCNT/$CsPbBr_3$ NC bilayer, baselined before illumination (dark), after photoexcitation at 405 nm for 10 min (light on), and after the 405 nm laser has been subsequently turned off for 12 min (light off).

anti-resonances at ca. 796 and 835 cm^{-1}, noted with asterisks, are noticeably absent in the (6,5) Raman spectrum. We hypothesized that these peaks could originate from the presence of the polyfluorene wrapping polymer. To test this hypothesis, we exchanged the PFO-BPy wrapping polymer with a cleavable supramolecular polymer, as described in our prior studies [28, 31]. As shown in Fig. S1 in the Electronic Supplementary Material (ESM), the 796 cm^{-1} peak and the 835 cm^{-1} peak almost entirely disappear for polymer-free (6,5) films, confirming that they originate from the presence of the wrapping polymer (see below for assignments).

Although prior studies exploring Fano resonances induced by charge carriers in graphene and s-SWCNTs have been restricted to chemically injected carriers [7, 26, 27], free carriers can also be generated by photoinduced charge separation [6, 24, 25, 29, 32]. In Fig. 1(c), we plot IR spectra of a type-II bilayer of (6,5) s-SWCNTs and $CsPbBr_3$ nanocrystals (NCs) under two conditions—after 10 min of continuous illumination (light-on) and after 12 min in the dark following the light-on period. As detailed in our recent study, photoexcitation of this bilayer system leads to interfacial charge separation and persistent conductivity [29]. Following charge separation, electrons residing in the NC layer and holes residing in the s-SWCNT layer remain separated for greater than

one hour and the s-SWCNT holes contribute to a large and persistent electrical conductivity. The free carrier absorption/anti-resonance spectrum for the excited-state photogenerated holes in this bilayer system is essentially identical to the spectrum observed for ground-state holes chemically injected by redox dopants, as similarly observed previously for semiconducting polymers [24, 25].

In Figs. 1(b) and 1(c), the D/G intensity ratio is greatly enhanced in the anti-resonances, relative to the Raman spectrum. Hertel et al. attributed the large enhancement of the D-band anti-resonance intensity to translational symmetry breaking and impurity scattering from a heterogeneous distribution of localized charge carriers [7]. Their study also found that the D-band intensity was largely diminished at high carrier densities. This effect was attributed to the restoration of translational symmetry for more homogeneous and delocalized carrier distributions associated with degenerate doping levels. Interestingly, we did not observe a progressive vanishing of the D-band anti-resonance at elevated carrier densities for our (6,5) s-SWCNT films.

To further test the possibility that the D-band anti-resonance vanishes for delocalized carriers in degenerately doped s-SWCNTs, we turned to thin films of large-diameter s-SWCNTs that were synthesized by the plasma torch (PT, Fig. 2) or LV (Fig. 3) methods. Carrier mobility scales roughly quadratically with the SWCNT diameter and the average diameter of plasma torch and laser vaporization SWCNTs (~ 1.4 nm) is almost twice that of (6,5) SWCNTs (~ 0.76 nm). Using plasma torch SWCNTs and another cleavable wrapping polymer (poly[(9,9-di-n-dodecyl-2,7-fluorendiyl-dimethine)-(1,4-phenylene-dinitrilomethine)] (PFPD), we have previously demonstrated the highest conductivities and thermoelectric power factors reported for enriched s-SWCNT networks [33]. Carrier density-dependent transport models have also been applied to our plasma torch and laser vaporization s-SWCNT thermoelectric results and suggest a clear transition from

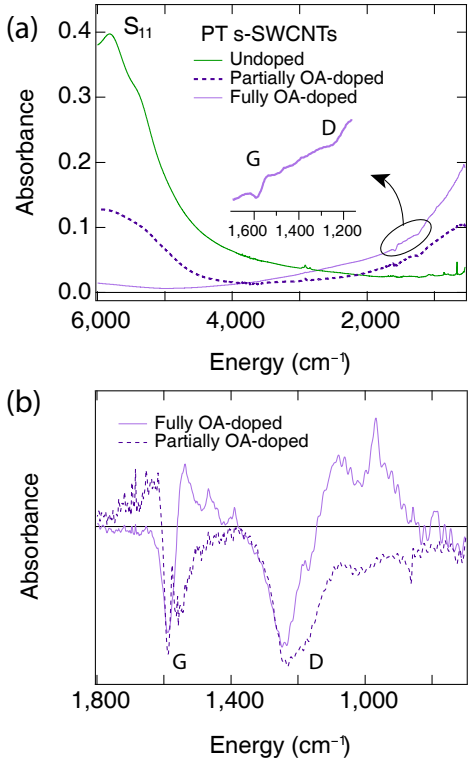

Figure 2 (a) FTIR spectra of undoped, partially doped and fully p-type doped plasma torch s-SWCNTs. The inset highlights the G- and D-band anti-resonances for the fully doped sample. (b) Free carrier absorption-subtracted FTIR spectra of the partially and fully doped plasma torch s-SWCNTs.

extrinsically limited transport at low carrier densities to "intrinsic" acoustic-phonon limited transport of delocalized carriers at high carrier densities [34, 35]. As such, degenerately doped plasma torch and laser vaporization s-SWCNT thin films represent well-vetted model systems to probe the spectroscopic signatures of delocalized carriers.

Figure 2(a) displays FTIR spectra of a plasma torch s-SWCNT film before and after doping with triethyloxonium hexachloroantimonate. The solid purple line shows the degenerately doped film, which has an exceptionally high direct current (DC) conductivity of ca. 6×10^5 S·m^{-1} [33]. The S_{11} excitonic transitions are completely bleached, as expected for degenerately doped s-SWCNTs. Clear anti-resonances for both the G- and D-bands can be observed in the zoomed inset and these peaks are further evident in the free carrier absorption-subtracted spectra shown in Fig. 2(b). Interestingly, the spectral shape of the fully doped (degenerate) film is substantially different than that of the partially doped spectrum. This change in shape is primarily related to the Fano parameter q in the Fano lineshape equation (see Fig. S2 in the ESM) and the potential implications of these differences are outside the scope of this study. Most importantly, Fig. 2 demonstrates that the D-band intensity remains strong and is typically more intense than the G-band intensity, even for ostensibly delocalized carriers in degenerately doped s-SWCNT networks.

To further probe the spectral signatures of delocalized carriers in highly conductive large-diameter nanotubes, we studied laser vaporization s-SWCNTs extracted with the cleavable supramolecular polymer [36]. Since close inspection and comparison of the G- and D-band anti-resonances requires the subtraction of the large free carrier absorption background, we wanted to ensure this subtraction procedure did not lead us to improperly assign features or amplify the intensity of the anti-resonance that we attribute to the D-band. Isotopically tuned s-SWCNTs with varying concentrations of ^{13}C are ideal for validating the spectral features [37], since the ^{13}C isotope effect should lead to a prescriptive bathochromic shift of the s-SWCNT vibrational modes. Figure 3(a) displays the FTIR and Raman spectra of s-SWCNT networks with varying concentrations of ^{13}C following polymer removal and degenerate p-type doping. As expected for the differences in atomic masses, the anti-resonances and Raman modes corresponding to the G-band and D-band regions display bathochromic shifts for the ^{13}C s-SWCNTs (Fig. 3(b)), according to $\omega_{^{13}C} = \omega_{^{12}C}\sqrt{m_{^{12}C}/m_{^{13}C}}$. This analysis provides confidence that the free carrier absorption subtraction procedure is robust and that (as observed for plasma torch s-SWCNTs) the D-band anti-resonance intensity of degenerately doped and highly conductive laser vaporization s-SWCNT networks is roughly equivalent to, or exceeds, the G-band intensity.

Another consistent observation is that for both plasma torch and laser vaporization s-SWCNT networks that were prepared with cleavable polymers, there are no anti-resonances observable at ca. 796 and 853 cm^{-1}. The absence of these peaks in all three samples prepared with a cleavable polymer further supports the conclusion that these peaks can be attributed to the presence of the wrapping polymer. Figure S3 in the ESM demonstrates that the 796 cm^{-1} peak is an IR-active PFO-BPy mode, while there is not a polymer peak near 853 cm^{-1} in the IR or Raman spectra. This peak position does match the expected range for the IR-active "radial" mode in ca. 0.76 nm diameter SWCNTs [38–40], and Lapointe et al. observed a very weak Fano resonance in this range for large-diameter SWCNTs [26]. This vibrational mode is analogous to the A_{2u} mode in graphite, but involves a radial twisting motion in the SWCNT [38]. Interestingly, the very strong intensity of the "radial" A_{2u} peak in doped (6,5) films in the

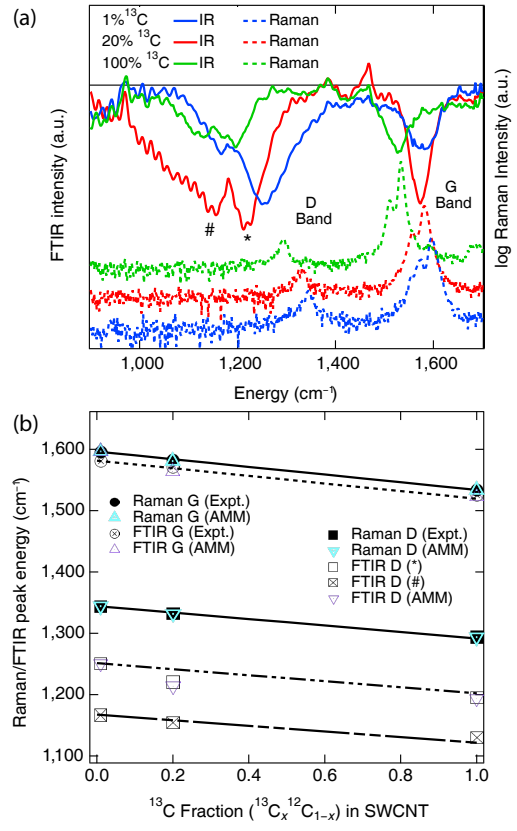

Figure 3 (a) Comparison of FTIR (solid) and Raman (dashed) spectra for degenerately doped laser vaporization s-SWCNTs with varying ^{13}C concentrations. Note that we use a log scale for the Raman spectra to ensure that the low-intensity D-band is easily visible. The * and # symbols denote the two dominant peaks associated with the D-band. (b) Shift of Raman or FTIR features with the isotopic ^{13}C fraction. The five trend lines represent the expected shift for each observed mode based on the inverse square root dependence on isotopic mass discussed in the text. Note that the low intensity of the weak D-band in these laser vaporization s-SWCNTs makes it challenging to identify the smaller (#) peak at lower energy that can be identified FTIR spectra (of both the laser vaporization and (6,5) s-SWCNTs).

presence of the wrapping polymer and its near-disappearance upon polymer removal (Fig. S1 in the ESM) suggest that the anti-resonance is enhanced by both (1) excess charge carriers and (2) coupling between the SWCNT and wrapping polymer.

We can briefly discuss the potential mechanism(s) giving rise to these two low-energy anti-resonances. First, we note that, in addition to observing the 796 cm^{-1} polymer mode at high carrier densities, it is also present (and strong) under doping or photoexcitation conditions where only low/moderate carrier densities are injected into the s-SWCNT network. As demonstrated in our previous study [41], the polymer itself is not doped in these conditions. The observation of the polymer-specific anti-resonance when the polymer is undoped suggests that it arises from coupling of the discrete polymer vibrational mode to the SWCNT free carrier continuum. In turn, this suggests that the polymer is in close physical contact with the SWCNT (as expected) and that electronic orbitals of the polymer may be strongly coupled, and potentially even hybridized to some degree (as suggested by some studies) [42], with SWCNT orbitals. The observation of a strong SWCNT-specific "radial" A_{2u} mode at 853 cm^{-1} only in the presence of the polymer suggests that this mode is strongly enhanced by this physical interaction. The symmetry of this mode suggests that the polymer may radially compress the SWCNT, as also suggested in our recent study [31]. We will explore these possibilities further in future studies.

The observation of strong D-band anti-resonances, even for degenerately doped samples identified previously as hosting highly delocalized carriers [34, 35], requires us to consider a distinct model to understand the relative intensities and underlying physics of the anti-resonance features. To better understand the impact of electron–phonon (e–p) coupling on the anti-resonances observed in our doped s-SWCNT thin films, we turn to a detailed analysis with the amplitude mode model [22, 24]. When the electronic system is subjected to strong e–p coupling, the phonon frequencies, as revealed in resonant Raman scattering and IR absorption spectra, become sensitive to the forces acting on the electrons. In general, the force constant that determines the phonon frequency is composed of the spring constant associated with the second derivative of the ion-ion repulsion potential, but also to the second derivative of the e–p related electronic energy. Therefore, the phonon frequencies become renormalized upon doping, photoexcitation, and phase transitions such as Peierls transition [15].

In previous applications of the model it has been explicitly assumed that the adiabatic approximation holds true [16–23]. This was a correct assumption since the Raman frequencies are much smaller than the energies of the electronic absorption bands. This approximation, however, does not hold in the case of doped s-SWCNTs, since the vibrational frequencies are in resonance with the free carrier absorption band of carriers introduced by the dopants. We thus need to use the modified amplitude mode model that includes non-adiabatic effects [24]. An important ingredient of the amplitude mode model is that all strongly coupled vibrations are interconnected by being coupled to the same phonon propagator. The bare phonon propagator in the 1D compound is given by [16–22]

$$D_0(\omega) = \sum_n \frac{\lambda_n}{\lambda} \frac{(\omega_n^0)^2}{\omega^2 - (\omega_n^0)^2 - i\omega\delta_n} \quad (1)$$

where ω_n^0, δ_n, and λ_n are the bare frequencies, their natural width, and e–p coupling constants, respectively; and $\Sigma\lambda_n = \lambda$, which is the total e–p coupling constant. The index n, which varies from 1 to N, describes the number of coupled modes in the SWCNT and we utilized $N = 4$ for the (6,5) SWCNT in the present study (three peaks for the G-band and one peak for the D-band). An example of the function $D_0(\omega)$is shown in Fig. 4(a) for (6,5) s-SWCNTs; it has poles at the four bare frequencies and reaches the value of –1 at $\omega = 0$. This is because at $\omega = 0$ the numerator and denominator in $D_0(\omega)$ cancel each other, and $\Sigma -\lambda_n/\lambda = -1$. Figure S4 in the ESM shows the calculated $D_0(\omega)$ function for the isotope-tuned LV s-SWCNTs.

We now turn to the e–p coupling. The bare frequencies in the e–p coupled SWCNT are renormalized, since they interact with the electronic energy gap, so that their modified propagator is given by a "Dyson-type" equation [15]

$$D(\omega) = \frac{D_0(\omega)}{1 + (1 - 2\lambda^*) D_0(\omega)} \quad (2)$$

where the renormalization parameter $2\lambda^* = (1 - 2\lambda E''(2\Delta_0))$, E'' is the second derivative of the total electron–phonon system vs. the total vibrational amplitude, Q. The poles of Eq. (2) are the renormalized Raman frequencies, ω_n^R of the SWCNT, given by the relation [15]

$$D_0(\omega) = -(1 - 2\lambda^*)^{-1} \quad (3)$$

This equation can be solved numerically and represented as the intersection of the function $D_0(\omega)$ and a horizontal line at a negative constant $y_R = -(1 - 2\lambda^*)^{-1}$ that may be treated as a fitting parameter.

Upon doping, the phonons are renormalized again to $\omega_{n,AR}$

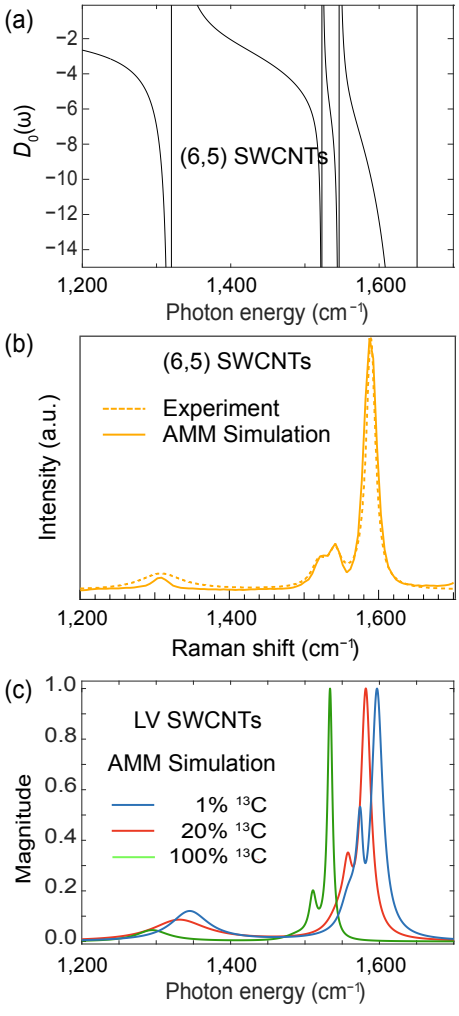

Figure 4 (a) Photon energy dependence of amplitude mode model phonon propagator, $D_0(\omega)$, for (6,5) s-SWCNTs, considering four distinct modes. (b) Comparison of amplitude mode model calculated (6,5) Raman spectrum (solid line) to experimental spectrum (dashed line). (c) Shift of amplitude mode model calculated laser vaporization Raman spectra as a function of ^{13}C isotope concentration. Peak positions are compared to experimental data in Fig. 3(b).

since the doping alters the electronic energy, and, in turn the e–p energy. In addition, doping also introduces an absorption band at low photon energy due to free carrier absorption, which is given by the Drude formula, where $\alpha_{FCA}(\omega) \sim \omega^{-2}$ (see Fig. 1). In this case, the doping modified phonons appear as anti-resonances at frequencies $\omega_{n,AR}$ lying on top of the free carrier absorption band. The $\omega_{n,AR}$ can be calculated from the zeroes of the conductivity (or absorption) response, $\sigma(\omega)$ [24]

$$\sigma(\omega) \sim \frac{1+D_0(\omega)(1-\alpha')}{1+D_0(\omega)[1+c1-\alpha]} \quad (4)$$

which are given by the relation

$$D_0(\omega) = -(1-\alpha')^{-1} \quad (5)$$

where α' is a non-adiabatic renormalization parameter and α is the pinning parameter [15, 17]. In principle, the frequencies $\omega_{n,AR}$ can be numerically obtained from Eq. (5), as represented by interception between the same $D_0(\omega)$ as for the Raman frequencies, but with a horizontal line at $y_{AR} = -(1-\alpha')^{-1}$ which is different from y_R for the Raman case.

To fit the various renormalized frequencies, we must find $2N-1$ parameters ($N = 4$) associated with $D_0(\omega)$, and two additional parameters, namely y_R and y_{AR}. This could be a formidable task in SWCNTs for which $N = 4$, since there are 9 unknown parameters and only 8 experimental frequencies (namely four Raman modes and four anti-resonances). Fortunately, consideration of the Raman intensities simplifies this task, as follows. One of the benefits of using the amplitude mode model to describe the most strongly coupled vibrations of the NT is that it can predict the relative scattering intensities in the Raman spectrum [22]. This is a unique virtue since, these relative intensities are typically rather challenging to predict. The reason behind this extraordinary ability is that all renormalized modes are related to each other through the same phonon propagator, which is not the case in Raman spectra of most usual compounds. It turns out that the Raman scattering intensity I_n of each renormalized mode is inversely proportional to the slope of $D_0(\omega)$ at the renormalized frequencies [22]; namely

$$I_n \sim |\mathrm{d}D_0(\omega)/\mathrm{d}\omega|^{-1} \text{ at } \omega = \omega_n^R \quad (6)$$

This property brings in four additional experimental values (in fact three relative intensities).

It is now straightforward to calculate the Raman scattering spectrum based on the amplitude mode model, as shown in Figs. 4(b) and 4(c). In Fig. 4(b), the calculated (6,5) Raman spectrum compares exceptionally well to the experimental spectrum, both in position and relative intensities. Figure 4(c) plots the calculated Raman spectra of laser vaporization SWCNTs with varying concentrations of the ^{13}C isotope. Here, we fit the Raman frequencies and intensities using bare frequencies that are different than those of ^{12}C SWCNT but kept the y_R and y_{AR} the same as for ^{12}C SWCNT since these values are related to the e–p electronic energy that is not susceptible to the isotope exchange. As expected, all three G-band peaks and the D-band experience bathochromic shifts with increasing ^{13}C concentration. As shown in Fig. 3(b), the calculated Raman shifts (blue triangles) are essentially identical to the experimentally observed Raman shifts, and both experiment and simulation agree with the expected mass square root relation.

The best fitting parameters for the (6,5) and the three isotopically varying laser vaporization SWCNT samples are given in Table S1 in the ESM. This analysis clearly shows that the NT experimental frequencies are renormalized by the e–p coupling in 1D. Furthermore, the good agreement between the simulation and experiment validates the assertion that the amplitude mode model is a reliable theoretical model for the vibrational frequencies in semiconducting SWCNTs.

In addition to zeroes in the conductivity spectrum in Eq. (4), there are also poles that occur at ω_n^P that are given by

$$D_0(\omega) = -(1+c1-\alpha)^{-1} = y_P \quad (7)$$

As with the Raman scattering poles, the conductivity poles may be obtained from the intersection of the function $D_0(\omega)$ with a horizontal line at y_P. Similar to the Raman scattering intensity given in Eq. (6), the intensity of the conductivity poles may be related to the inverse of the $D_0(\omega)$ derivative at ω_n^P. In reality, there is a distribution in the respective y-values, y_{AR} and y_P, which in turn results in a distribution of $\omega_{n,AR}$ and ω_n^P. In addition, y_{AR} and y_P may be very close to each other. These result in "smearing" of the anti-resonances and poles; namely the anti-resonances do not reach zero and the poles do not diverge. Taking these properties into account allows us the relate the strength of the anti-resonance dips to the poles intensity, and thus the anti-resonance intensity may be also related to the inverse of the $D_0(\omega)$ derivative at $\omega_{n,AR}$.

Figure 5 shows FTIR anti-resonance spectra calculated for (6,5) s-SWCNTs (Fig. 5(a)) and laser vaporization s-SWCNTs (Fig. 5(b)) by the amplitude mode model. The predominant observation from Fig. 5 is the outsized intensity of the D band relative to the highest energy G mode (labeled G_1, that

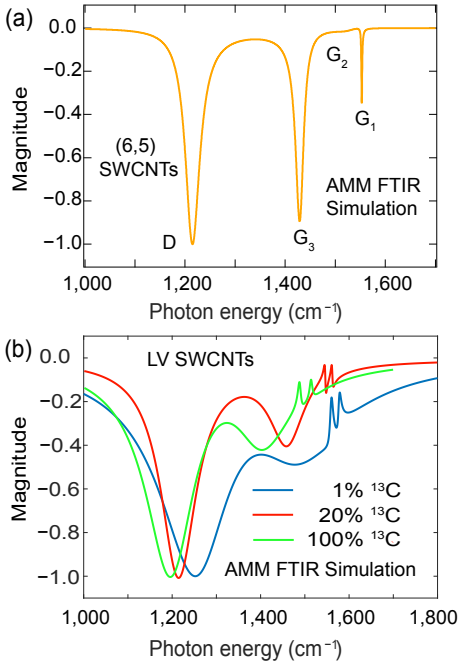

Figure 5 (a) Amplitude mode model calculated FTIR spectrum of doped (6,5) SWCNTs, showing anti-resonances arising from the three G peaks (G_1, G_2, and G_3) and one D peak. (b) Amplitude mode model calculated FTIR spectra of doped laser vaporization SWCNTs with different concentrations of ^{13}C isotope.

corresponds to the dominant G^+ mode). The large/small intensity of the D/G^+ band anti-resonance peaks in Fig. 5(a) is a direct result of the small/large derivative of $D_0(\omega)$ at $\omega_{n,AR}$ for each of these peaks. The second important observation from Fig. 5(b) is that the anti-resonance peak energies of both the D band and G band track well with the ^{13}C concentration in laser vaporization SWCNTs (purple triangles, Fig. 3(b)). These two observations suggest that the model can reliably capture the general trends in both the intensity ratios and energies of Raman spectral features and anti-resonances in FTIR spectra.

There are several important conclusions that can be gleaned from comparison of our experimental data to that simulated by amplitude mode model, as well as several caveats and opportunities for further refinement. First, while the D/G intensity ratio in the calculated anti-resonance spectrum is larger than that typically observed experimentally, the model captures the general trend that the D mode intensity is dramatically enhanced in the FTIR spectrum, relative to the D mode Raman intensity. Importantly, this suggests that the outsized contribution of the D band to the anti-resonance spectrum is a natural outcome of the shape and dispersion of the phonon propagator. Combined with the observation of very large D band anti-resonances for degenerately doped large-diameter s-SWCNTs with exceptionally large DC conductivity [33, 36] (Figs. 2 and 3), this result suggests that the D band anti-resonance intensity is not necessarily a reliable indicator of the relative extent of charge carrier localization. The diminishment of the D band anti-resonance intensity at high (6,5) s-SWCNT carrier densities in a prior study [7], in contrast to the lack of such diminishment in (6,5), laser vaporization, and plasma torch s-SWCNTs in this study, is an interesting discrepancy that warrants further study.

Some additional refinements may also enable the amplitude mode model to capture the D/G anti-resonance intensity ratio more accurately, as well as several "minor" mode frequencies and intensities. One obvious shortcoming is the emergence of fine structure within the experimentally observed D band that is not captured with the current implementation, since the amplitude mode model was populated with only one D peak (as resolved in Raman spectra). However, diameter polydispersity, trigonal warping, and other effects can induce several sub-bands within the D band [43], and this fine structure is apparently substantially more prominent in the strong anti-resonances observed here (e.g., Figs. 1(b), 2(b), and 3(a)) than in the Raman spectra with low-intensity D bands. Capturing the relative anti-resonance intensities more accurately also requires deeper knowledge of the frequency dispersion of each phonon mode with excitation photon energy, which enables a more precise representation of the $D_0(\omega)$ function. Such dispersion curves do not exist for near-monochiral (6,5) s-SWCNTs and have rarely been captured for any samples at excitation photon energies below the S_{22} excitonic transition.

Finally, we note that the current implementation of the amplitude mode model on the (6,5) s-SWCNTs does not include the contribution of PFO-BPy vibrational modes. Figure S1 in the ESM clearly shows that the peak at ca. 796 cm^{-1} corresponds to a PFO-BPy mode, but Fig. S2 in the ESM shows several other peaks in the PFO-BPy Raman and IR spectra that may contribute to the overall anti-resonance spectrum of the doped s-SWCNTs. Importantly, the maximum shift of each mode in the $D_0(\omega)$ function is constrained by a neighboring mode with lower frequency. As such, the clear coupling of wrapping polymer modes to the s-SWCNT free carrier continuum means that these modes may impact both the ultimate frequency shift and intensity ratios of the anti-resonances observed for the SWCNT modes.

Acknowledgements

This work was authored by the National Renewable Energy Laboratory (NREL), operated by Alliance for Sustainable Energy, LLC, for the U.S. Department of Energy (DOE) under Contract No. DE-AC36-08GO28308. Separation, doping, and spectroscopy of SWCNTs was supported by the Solar Photochemistry Program, Division of Chemical Sciences, Geosciences, and Biosciences, Office of Basic Energy Sciences, U.S. DOE. Fabrication and characterization of SWCNT-perovskite heterostructures and development and application of the amplitude mode model to SWCNT spectra was supported as part of the Center for Hybrid Organic Inorganic Semiconductors for Energy (CHOISE), an Energy Frontier Research Center funded by the Office of Science, Basic Energy Sciences within the US. DOE. S. R. V. and Z. V. V. acknowledge support for the amplitude mode model theoretical study from the DOE Office of Science, No. DE-SC0014579. S. R. V. was partially supported by the JSPS KAKENHI Number 20H00391, 21K18722.

Electronic Supplementary Material: Supplementary material (the Experimental methods; FTIR comparison of PFO-BPy wrapped and polymer-removed p-type doped (6,5) SWCNT films; FTIR and Raman spectra of PFO-BPy; and best fit parameters for amplitude mode model fits) is available in the online version of this article at https://doi.org/10.1007/s12274-022-5080-1.

References

[1] Habisreutinger, S. N.; Blackburn, J. L. Carbon nanotubes in high-performance perovskite photovoltaics and other emerging optoelectronic applications. *J. Appl. Phys.* **2021**, *129*, 010903.
[2] Massetti, M.; Jiao, F.; Ferguson, A. J.; Zhao, D.; Wijeratne, K.; Würger, A.; Blackburn, J. L.; Crispin, X.; Fabiano, S. Unconventional thermoelectric materials for energy harvesting and sensing applications. *Chem. Rev.* **2021**, *121*, 12465–12547.
[3] Peng, L. M.; Zhang, Z. Y.; Qiu, C. G. Carbon nanotube digital electronics. *Nat. Electron.* **2019**, *2*, 499–505.
[4] Hao, J.; Nanayakkara, S. U.; Tervo, E. J.; Blackburn, J. L.; Ferguson, A. J. High-performance carbon nanotube electronic ratchets. *Energy*

Environ. Sci. **2021**, *14*, 5457–5468.
[5] Zorn, N. F.; Zaumseil, J. Charge transport in semiconducting carbon nanotube networks. *Appl. Phys. Rev.* **2021**, *8*, 041318.
[6] Blackburn, J. L.; Ferguson, A. J.; Reid, O. G. Chapter 14: Spectroscopy of ground- and excited-state charge carriers in single-wall carbon nanotubes. In *Handbook of Carbon Nanomaterials*; Weisman, R. B., Kono, J., Eds.; World Scientific Publishing Company: Hackensack, 2019; pp 237–296.
[7] Eckstein, K. H.; Hirsch, F.; Martel, R.; Hertel, T. Infrared study of charge carrier confinement in doped (6,5) carbon nanotubes. *J. Phys. Chem. C* **2021**, *125*, 5700–5707.
[8] Park, J.; Reid, O. G.; Blackburn, J. L.; Rumbles, G. Photoinduced spontaneous free-carrier generation in semiconducting single-walled carbon nanotubes. *Nat. Commun.* **2015**, *6*, 8809.
[9] Burdanova, M. G.; Tsapenko, A. P.; Kharlamova, M. V.; Kauppinen, E. I.; Gorshunov, B. P.; Kono, J.; Lloyd-Hughes, J. A review of the terahertz conductivity and photoconductivity of carbon nanotubes and heteronanotubes. *Adv. Opt. Mater.* **2021**, *9*, 2101042.
[10] Eckstein, K. H.; Oberndorfer, F.; Achsnich, M. M.; Schöppler, F.; Hertel, T. Quantifying doping levels in carbon nanotubes by optical spectroscopy. *J. Phys. Chem. C* **2019**, *123*, 30001–30006.
[11] Hertel, T. Chapter 13: Optical spectroscopy of doped carbon nanotubes. In *Handbook of Carbon Nanomaterials*; Weisman, R. B. , Kono, J. , Eds; World Scientific: Hackensack, 2019; pp 191–236.
[12] Mansour, A. E.; Lungwitz, D.; Schultz, T.; Arvind, M.; Valencia, A. M.; Cocchi, C.; Opitz, A.; Neher, D.; Koch, N. The optical signatures of molecular-doping induced polarons in poly(3-Hexylthiophene-2,5-diyl): Individual polymer chains versus aggregates. *J. Mater. Chem. C* **2020**, *8*, 2870–2879.
[13] Spano, F. C. The spectral signatures of frenkel polarons in H- and J-aggregates. *Acc. Chem. Res.* **2010**, *43*, 429–439.
[14] Zaumseil, J. Semiconducting single-walled carbon nanotubes or very rigid conjugated polymers: A comparison. *Adv. Electron. Mater.* **2019**, *5*, 1800514.
[15] Horovitz, B. Infrared activity of peierls systems and application to polyacetylene. *Solid State Commun.* **1982**, *41*, 729–734.
[16] Vardeny, Z.; Ehrenfreund, E.; Brafman, O.; Horovitz, B. Resonant Raman scattering from amplitude modes in trans-$(CH)_x$ and -$(CD)_x$. *Phys. Rev. Lett.* **1983**, *51*, 2326–2329.
[17] Vardeny, Z. Photoinduced Ir-active vibrations in trans-$(CD)_x$: A three-mode system. *Phys. Rev. Lett.* **1983**, *51*, 1221.
[18] Vardeny, Z.; Orenstein, J.; Baker, G. L. Photoinduced infrared activity in polyacetylene. *Phys. Rev. Lett.* **1983**, *50*, 2032–2035.
[19] Brafman, O.; Vardeny, Z.; Ehrenfreund, E. Isotope effect in resonant Raman scattering and induced IR spectra of trans-polyacetylene. *Solid State Commun.* **1985**, *53*, 615–619.
[20] Vardeny, Z.; Ehrenfreund, E.; Brafman, O.; Horovitz, B. Classification of disorder and extrinsic order in polymers by resonant Raman scattering. *Phys. Rev. Lett.* **1985**, *54*, 75–78.
[21] Horovitz, B.; Vardeny, Z.; Ehrenfreund, E.; Brafman, O. Raman scattering from charge-density waves and application to polyacetylene. *J. Phys. C: Solid State Phys.* **1986**, *19*, 7291–7305.
[22] Ehrenfreund, E.; Vardeny, Z.; Brafman, O.; Horovitz, B. Amplitude and phase modes in *trans*-polyacetylene: Resonant Raman scattering and induced infrared activity. *Phys. Rev. B* **1987**, *36*, 1535–1553.
[23] Ozaki, M.; Ehrenfreund, E.; Benner, R. E.; Barton, T. J.; Yoshino, K.; Vardeny, Z. V. Dispersion of resonant Raman scattering in π-conjugated polymers: Role of the even parity excitons. *Phys. Rev. Lett.* **1997**, *79*, 1762–1765.
[24] Österbacka, R.; Jiang, X. M.; An, C. P.; Horovitz, B.; Vardeny, Z. V. Photoinduced quantum interference antiresonances in π-conjugated polymers. *Phys. Rev. Lett.* **2002**, *88*, 226401.
[25] Baniya, S.; Vardeny, S. R.; Lafalce, E.; Peygambarian, N.; Vardeny, Z. V. Amplitude-mode spectroscopy of charge excitations in PTB7 π-conjugated donor-acceptor copolymer for photovoltaic applications. *Phys. Rev. Appl.* **2017**, *7*, 064031.
[26] Lapointe, F.; Gaufrès, É.; Tremblay, I.; Tang, N. Y. W.; Martel, R.; Desjardins, P. Fano resonances in the midinfrared spectra of single-walled carbon nanotubes. *Phys. Rev. Lett.* **2012**, *109*, 097402.
[27] Lapointe, F.; Rousseau, B.; Aymong, V.; Nguyen, M.; Biron, M.; Gaufrès, E.; Choubak, S.; Han, Z.; Bouchiat, V.; Desjardins, P. et al. Antiresonances in the mid-infrared vibrational spectrum of functionalized graphene. *J. Phys. Chem. C* **2017**, *121*, 9053–9062.
[28] Ferguson, A. J.; Reid, O. G.; Nanayakkara, S. U.; Ihly, R.; Blackburn, J. L. Efficiency of charge-transfer doping in organic semiconductors probed with quantitative microwave and direct-current conductance. *J. Phys. Chem. Lett.* **2018**, *9*, 6864–6870.
[29] Hao, J.; Kim, Y. H.; Habisreutinger, S. N.; Harvey, S. P.; Miller, E. M.; Foradori, S. M.; Arnold, M. S.; Song, Z. N.; Yan, Y. F.; Luther, J. M. et al. Low-energy room-temperature optical switching in mixed-dimensionality nanoscale perovskite heterojunctions. *Sci. Adv.* **2021**, *7*, eabf1959.
[30] Matsunaga, R.; Matsuda, K.; Kanemitsu, Y. Observation of charged excitons in hole-doped carbon nanotubes using photoluminescence and absorption spectroscopy. *Phys. Rev. Lett.* **2011**, *106*, 037404.
[31] Arias, D. H.; Sulas-Kern, D. B.; Hart, S. M.; Kang, H. S.; Hao, J.; Ihly, R.; Johnson, J. C.; Blackburn, J. L.; Ferguson, A. J. Effect of nanotube coupling on exciton transport in polymer-free monochiral semiconducting carbon nanotube networks. *Nanoscale* **2019**, *11*, 21196–21206.
[32] Blackburn, J. L. Semiconducting single-walled carbon nanotubes in solar energy harvesting. *ACS Energy Lett.* **2017**, *2*, 1598–1613.
[33] MacLeod, B. A.; Stanton, N. J.; Gould, I. E.; Wesenberg, D.; Ihly, R.; Owczarczyk, Z. R.; Hurst, K. E.; Fewox, C. S.; Folmar, C. N.; Hughes, K. H. et al. Large N- and P-type thermoelectric power factors from doped semiconducting single-walled carbon nanotube thin films. *Energy Environ. Sci.* **2017**, *10*, 2168–2179.
[34] Blackburn, J. L.; Kang, S. D.; Roos, M. J.; Norton-Baker, B.; Miller, E. M.; Ferguson, A. J. Intrinsic and extrinsically limited thermoelectric transport within semiconducting single-walled carbon nanotube networks. *Adv. Electron. Mater.* **2019**, *5*, 1800910.
[35] Gregory, S. A.; Hanus, R.; Atassi, A.; Rinehart, J. M.; Wooding, J. P.; Menon, A. K.; Losego, M. D.; Snyder, G. J.; Yee, S. K. Quantifying charge carrier localization in chemically doped semiconducting polymers. *Nat. Mater.* **2021**, *20*, 1414–1421.
[36] Norton-Baker, B.; Ihly, R.; Gould, I. E.; Avery, A. D.; Owczarczyk, Z. R.; Ferguson, A. J.; Blackburn, J. L. Polymer-free carbon nanotube thermoelectrics with improved charge carrier transport and power factor. *ACS Energy Lett.* **2016**, *1*, 1212–1220.
[37] Engtrakul, C.; Davis, M. F.; Mistry, K.; Larsen, B. A.; Dillon, A. C.; Heben, M. J.; Blackburn, J. L. Solid-state ^{13}C nmr assignment of carbon resonances on metallic and semiconducting single-walled carbon nanotubes. *J. Am. Chem. Soc.* **2010**, *132*, 9956–9957.
[38] Zhou, J.; Dong, J. M. Infrared properties of single-walled carbon nanotubes calculated from first principles. *J. Appl. Phys.* **2010**, *107*, 024306.
[39] Pekker, Á.; Botos, Á.; Rusznyák, Á.; Koltai, J.; Kürti, J.; Kamarás, K. Vibrational signatures in the infrared spectra of single- and double-walled carbon nanotubes and their diameter dependence. *J. Phys. Chem. Lett.* **2011**, *2*, 2079–2082.
[40] Dobardžić, E.; Milošević, I.; Nikolić, B.; Vuković, T.; Damnjanović, M. Single-wall carbon nanotubes phonon spectra: Symmetry-based calculations. *Phys. Rev. B* **2003**, *68*, 045408.
[41] Avery, A. D.; Zhou, B. H.; Lee, J.; Lee, E. S.; Miller, E. M.; Ihly, R.; Wesenberg, D.; Mistry, K. S.; Guillot, S. L.; Zink, B. L. et al. Tailored semiconducting carbon nanotube networks with enhanced thermoelectric properties. *Nat. Energy* **2016**, *1*, 16033.
[42] Kahmann, S.; Rios, J. M. S.; Zink, M.; Allard, S.; Scherf, U.; Dos Santos, M. C.; Brabec, C. J.; Loi, M. A. Excited-state interaction of semiconducting single-walled carbon nanotubes with their wrapping polymers. *J. Phys. Chem. Lett.* **2017**, *8*, 5666–5672.
[43] Zólyomi, V.; Kürti, J.; Grüneis, A.; Kuzmany, H. Origin of the fine structure of the Raman *D* band in single-wall carbon nanotubes. *Phys. Rev. Lett.* **2003**, *90*, 157401.